On the sound fields of oblate and prolate hemispheroids in infinite baffles for directivity control

Tim Mellow[1] and Leo Kärkkäinen[2,a)]

[1]*Mellow Acoustics Ltd., 42 Hale Road, Farnham Surrey GU9 9QH, United Kingdom*

[2]*Aalto University, Otakaari 1B 02150, Espoo, Finland*

ABSTRACT:

The hemispheroid is presented as an apodized form for controlling the beam width of a sound source by varying its height-to-radius ratio. Directivity patterns, on-axis responses, and radiation impedances are calculated for various height-radius ratios of the oblate hemispheroid using spheroidal wave functions. It turns out that, for smaller angles at least, there is a direct relationship between the internal angle of the semi-elliptic cross section and the half-cone angle within which the far-field pressure is largely contained at high frequencies. The hemispheroid is compared with both a spherical cap, which produces a much less regular response, and a high-frequency asymptotic approximation. The high-frequency asymptotic approximation is in the form of a flat circular radiator with a delay that increases radially from the center to the perimeter, as used in some electrostatic loudspeakers. With the almost complete absence of lobes, this appears to be an effective alternative means of apodization to a shaded array and is more efficient because, unlike a shaded array, constant axial velocity is maintained over the whole surface. A high-frequency approximation is also derived for a prolate hemispheroid. Since this may be formed from a planar array, a beam steering option is added. © *2021 Acoustical Society of America*. https://doi.org/10.1121/10.0006730

I. INTRODUCTION

There are essentially two methods for broadening the beam width (i.e., central lobe of the directivity pattern) of a sound source at high frequencies where the wavelength is several times smaller than the width of the source. One is to employ a planar array of sources with different amounts of electronic delay applied to each to obtain the desired pattern. Amplitude "shading" is often applied to those closer to the edge to avoid response irregularities and unwanted side lobes in the directivity pattern.

However, a simpler method is to use a source with a curved radiating surface, although making it rigid enough to avoid breakup resonances in its working frequency range is a challenge. Hence, exotic materials, such as beryllium and diamond, have been used. Here, we shall assume it to be perfectly rigid so that we can examine the sound radiation due to the geometry of the source in isolation from the material properties. A well-known form is the spherical cap in an infinite baffle, as shown in Fig. 1(a), which has radius a and height b. The center-angle of the arc formed by the cap is 2α. Many hi-fi tweeters and Bluetooth speakers approximate this form. A mathematical approximation is devised by Kates,[1] which assumes a planar surface with a progressively increasing axial delay towards the rim. This provides a good approximation when the wavelength is much smaller than the diameter of the cap but a more rigorous treatment by Suzuki and Tichy[2] accounts for the effect of the physical geometry when the wavelength is closer to the

diameter. Beranek and Mellow[3] simplify the latter model by applying the property of orthogonality to eliminate the need for the least-mean-squares algorithm.

The effect of the spherical cap on the directivity pattern is to contain the high-frequency radiation largely within the half-cone angle α, as seen from Figs. 2(a) and 2(b) for $\alpha = 30°$ and $15°$, respectively, which are calculated from Eq. (12.137) of Ref. 3.

We see from Fig. 1(b) that, due to the reflection in the baffle, the cap is equivalent to two back-back caps oscillating in opposite directions in free space. There is a discontinuity where they join at the perimeter $(x = a)$ which produces notches in the on-axis response that deepen with decreasing α, as seen in Fig. 3. The on-axis response of the hemispherical cap $(\alpha = \pi/2)$, however, is fairly smooth because there is continuity where the two hemispheres join. We may think of the spherical cap as an unshaded array, whereas the hemispherical cap is "self-shading" because its geometry produces zero normal velocity at the rim. This, in turn, has a smoothing effect on the far-field pressure.

An alternative to the spherical cap, which avoids this problem, is the oblate hemispheroid in an infinite baffle, the geometry of which is shown in Fig. 4(a). Again, it has radius a on the radial w-axis and height b on the axial z-axis. However, the profile is now an ellipse, instead of an arc, as described by the equation

$$z = b\sqrt{1 - \frac{w^2}{a^2}}, \tag{1}$$

a)Electronic mail: leo.karkkainen@aalto.fi, ORCID: 0000-0001-8228-6265.
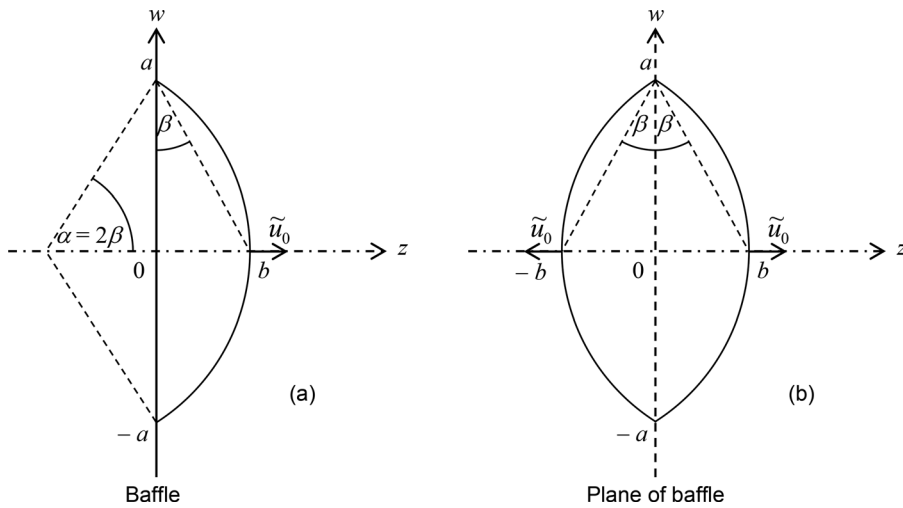
FIG. 1. Geometry of the spherical cap.

which is rotated about the z-axis. Like the spherical cap, we can model the hemispheroid as two back-to-back hemispheroids oscillating in opposite directions along the z-axis, which forms the axis of symmetry, as shown in Fig. 4(b). However, unlike the spherical cap, we see that for any height b, there is continuity where the two hemispheroids meet.

As mentioned earlier, the challenge with spherical caps and oblate hemispheroids is making them sufficiently rigid. The high-frequency approximation offers an alternative approach which may be realized by a planar source in which the radiating surface is divided into concentric rings fed by a suitable delay line to artificially create the desired profile. Walker[4] uses this, together with a flexible diaphragm, to

create a virtual (shaded) spherical cap, albeit a dipole pressure source as opposed to the rigid monopole source shown in Fig. 1. A similar scheme is also used to create a virtual oscillating sphere,[3] which is the dipole counterpart of the hemisphere or oblate hemispheroid when $\beta = 45°$.

In Sec. II of this paper, we formulate the oblate hemispheroid using axisymmetric spheroidal wave functions which are solutions to the separable Helmholtz wave equation in oblate spheroidal coordinates. Three methods have previously been used to normalize the angular spheroidal functions. Flammer[5] matches the value to that of a Legendre function when the argument is zero, whereas Stratton et al.,[6] do this for unity argument. However, for problems of practical importance, it is more useful to normalize them such that
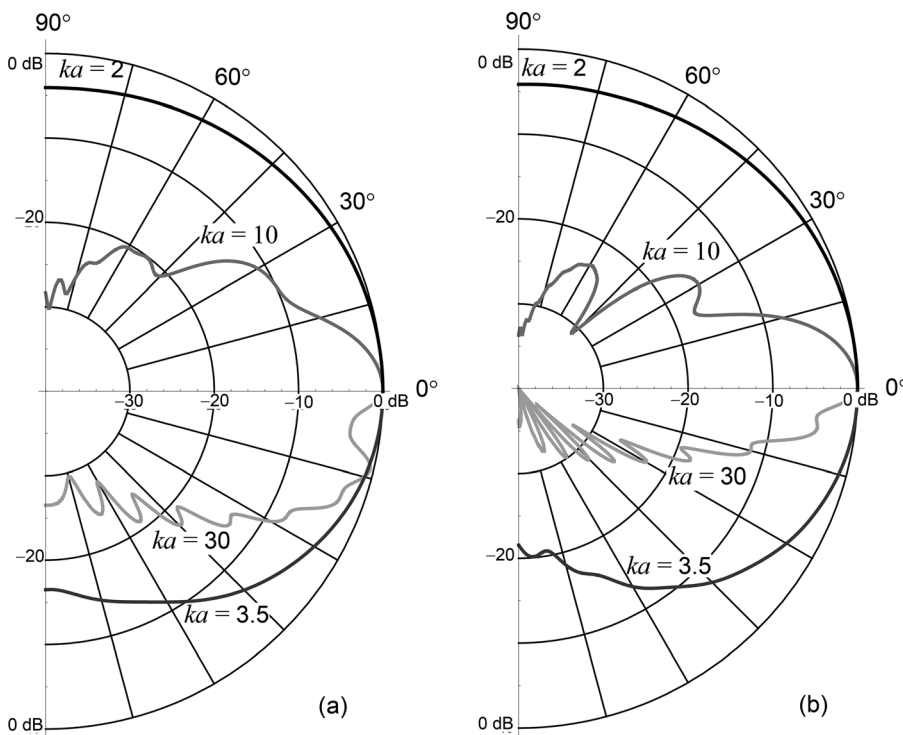

FIG. 2. Directivity patterns of the far-field pressure for the spherical cap for $\alpha = 30°$ (a) and $\alpha = 15°$ (b).
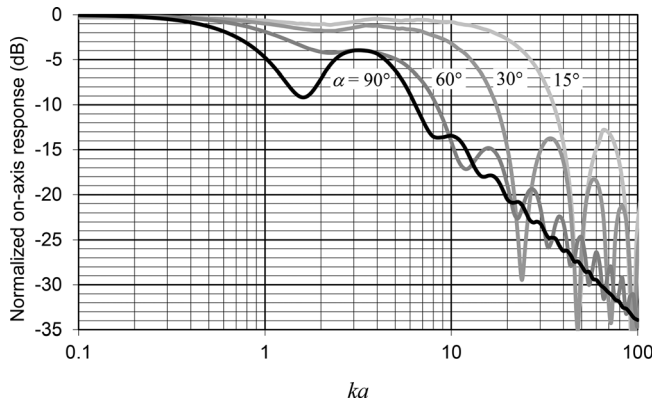
Tim Mellow and Leo Kärkkäinen

FIG. 3. On-axis pressure of a spherical cap in an infinite baffle for $\alpha = 15°$, $30°$, $60°$, and $90°$, respectively.

the orthogonal integral of a pair of spheroidal functions matches that of a pair of Legendre functions. The latter is the approach adopted by Meixner and Schäfke[7] and is also used here. The other advantage of their formulation is that separate formulas are not required for functions of odd and even order. Furthermore, they may even be expressed with fractional order. Hence, the Meixner and Schäfke formulation and notation is adopted throughout this derivation, which makes it directly compatible with mathematical software applications such as Mathematica®. The latter is based on the work of Falloon et al.[8] Van Buren also provides valuable programming techniques based on the Flammer formulation.[9]

We calculate the on-axis responses and directivity patterns of the far-field pressure, as well as the radiation impedance, for oblate hemispheroids of various aspect ratios b/a. We also calculate the far-field pressure using the high-frequency approximation for comparison. In Sec. III, we calculate the directivity patterns of a prolate hemispheroid, using the high-frequency approximation only, as a means of controlling the directivity independently in two perpendicular planes. Since it is relatively simple and illustrative to do so, we show directivity patterns for a few steering angles.
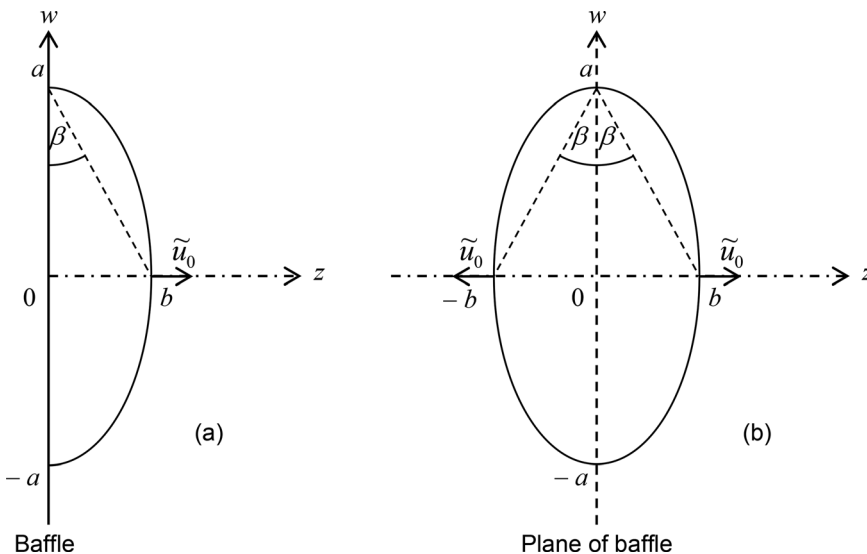
II. FAR-FIELD PRESSURE AND RADIATION IMPEDANCE OF AN OBLATE HEMISPHEROID INCLUDING HIGH-FREQUENCY APPROXIMATION

A. Boundary conditions

The symmetry of the configuration of Fig. 4(b) automatically satisfies the boundary condition of zero pressure gradient in the plane of the baffle

$$\frac{\partial}{\partial z}\tilde{p}(w,z) = 0, \quad a \leq w \leq \infty. \tag{2}$$

We use an oblate spheroidal coordinate system in η and ξ that fits the geometry of the problem as shown in Fig. 5, where

$$d = \sqrt{a^2 - b^2}. \tag{3}$$

The outline of the hemispheroid is an ellipse that intersects the z-axis at

$$\xi_{ab} = \frac{b}{d} = \frac{q}{\sqrt{1-q^2}}, \quad 0 \leq q < 1, \tag{4}$$

where

$$q = b/a \tag{5}$$

is the aspect ratio.

B. Near-field pressure

The pressure field due to the oblate hemispheroid is described in axisymmetric oblate spheroidal coordinates by

$$\tilde{p}(\xi,\eta) = \rho_0 c \tilde{u}_0 \sum_{n=0}^{N} A_n S_n^{(4)}(-i\gamma, i\xi) \mathrm{ps}_n(-i\gamma, \eta), \tag{6}$$

where $\gamma = kd$, $d = a\sqrt{1-q^2}$, $k = \omega/c = 2\pi f/c$ is the wave number, $\tilde{u}_0$ is the velocity in the z direction, ρ_0 is the density

FIG. 4. Geometry of the oblate hemispheroid.

J. Acoust. Soc. Am. **150** (4), October 2021

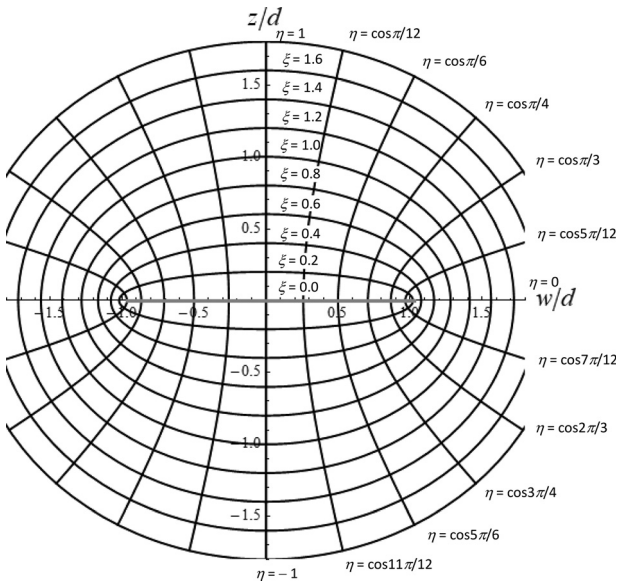Tim Mellow and Leo Kärkkäinen   3049

FIG. 5. Oblate spheroidal coordinate system.

of air, c is the speed of sound, and A_n are the unknown expansion coefficients to be determined. Also, $S_n^{(4)}$ and ps_n are the radial and angular oblate spheroidal wave functions,[7] which are defined in the Appendix. The angular and radial spheroidal ordinates η and ξ are related to the radial and axial cylindrical ordinates w and z by

$$w = \sqrt{(\xi^2 + 1)(1 - \eta^2)}\, d, \tag{7}$$

$$z = \xi \eta d. \tag{8}$$

The normal component of the particle velocity at the surface of the hemispheroid is then given by

$$
\begin{aligned}
\tilde{u}(\xi_{ab}, \eta) &= \frac{1}{-ik\rho_0 c} \frac{1}{d} \sqrt{\frac{\xi^2 + 1}{\xi^2 + \eta^2}} \frac{\partial}{\partial \xi} \tilde{p}(\xi, \eta)|_{\xi=\xi_{ab}} \\
&= \frac{1}{-i\gamma} \sqrt{\frac{\xi_{ab}^2 + 1}{\xi_{ab}^2 + \eta^2}} \tilde{u}_0 \\
&\quad \times \sum_{n=0}^{N} A_n S_n^{\prime(4)}(-i\gamma, i\xi_{ab}) \mathrm{ps}_n(-i\gamma, \eta) \\
&= \tilde{u}_0 |\eta| \sqrt{\frac{\xi_{ab}^2 + 1}{\xi_{ab}^2 + \eta^2}}, \quad -1 \le \eta \le 1. \tag{9}
\end{aligned}
$$

Note that we have included the scale factor[5] $\sqrt{(\xi^2 + 1)/(\xi^2 + \eta^2)}/d$ for the component of the pressure gradient that is normal to the hemispheroid. The absolute value of η in the third line accounts for the fact that the axial velocity is in the positive z direction on the front surface and in the $-z$ direction on the rear surface. Multiplying through by the normalizing function $\mathrm{ps}_m(-i\gamma, \eta)$ and integrating over η gives

$$
\frac{1}{-i\gamma} \sum_{n=0}^{\infty} A_n S_n^{\prime(4)}(-i\gamma, i\xi_{ab}) \int_{-1}^{1} \mathrm{ps}_m(-i\gamma, \eta) \mathrm{ps}_n(-i\gamma, \eta) d\eta
$$

$$
= \int_0^1 \mathrm{ps}_m(-i\gamma, \eta) \eta d\eta - \int_{-1}^0 \mathrm{ps}_m(-i\gamma, \eta) \eta d\eta, \tag{10}
$$

where we apply the orthogonal integral identity of Eq. (A20) together with

$$
\int_0^1 \mathrm{ps}_m(-i\gamma, \eta) \eta d\eta - \int_{-1}^0 \mathrm{ps}_m(-i\gamma, \eta) \eta d\eta
$$

$$
= \begin{cases} 0, & m \text{ odd} \\ 2 \int_0^1 \mathrm{ps}_m(-i\gamma, \eta) \eta d\eta, & m \text{ even.} \end{cases} \tag{11}
$$

Hence,

$$
A_n = \begin{cases} 0, & n \text{ odd} \\ -i \dfrac{(2n+1)\gamma}{S_n^{\prime(4)}(-i\gamma, i\xi_{ab})} \displaystyle\int_0^1 \mathrm{ps}_n(-i\gamma, \eta) \eta d\eta, & n \text{ even,} \end{cases} \tag{12}
$$

so that, after inserting this into Eq. (6), the near-field pressure becomes

$$
\begin{aligned}
\tilde{p}(\xi, \eta) &= -i\gamma \rho_0 c \tilde{u}_0 \sum_{n=0}^{N} (4n+1) I_{2n}(-i\gamma) \\
&\quad \times \frac{S_{2n}^{(4)}(-i\gamma, i\xi)}{S_{2n}^{\prime(4)}(-i\gamma, i\xi_{ab})} \mathrm{ps}_{2n}(-i\gamma, \eta), \tag{13}
\end{aligned}
$$

where

$$
I_{2n}(-i\gamma) = \int_0^1 \mathrm{ps}_{2n}(-i\gamma, \eta_0) \eta_0 d\eta_0, \tag{14}
$$

$$
\mathrm{ps}_{2n}(-i\gamma, \eta_0) = \sigma_{2n}(-i\gamma) \sum_{r=-n}^{R} (-1)^r u_{2n,r}(-i\gamma) P_{2n+2r}(\eta_0), \tag{15}
$$

where the normalization factors σ_{2n} and expansion coefficients $u_{2n,r}$ are given by Eqs. (A21) and (A6), respectively, and[10]

$$
\int_0^1 P_{2n+2r}(\eta_0) \eta_0 d\eta_0 = \frac{(-1)^{n+r+1} \Gamma\left(n+r-\dfrac{1}{2}\right)}{4\sqrt{\pi}\,\Gamma(n+r+2)} \tag{16}
$$

so that

$$
I_{2n}(-i\gamma) = \frac{(-1)^{n+1}}{4\sqrt{\pi}} \sigma_{2n}(-i\gamma) \sum_{r=-n}^{R} \frac{\Gamma\left(n+r-\dfrac{1}{2}\right)}{\Gamma(n+r+2)} u_{2n,r}(-i\gamma). \tag{17}
$$

Tim Mellow and Leo Kärkkäinen

C. Far-field pressure

Far large arguments, we use the relationship of Eq. (A16) so that

$$S_{2n}^{(4)}(-i\gamma, i\xi)|_{\xi\to\infty} = i\frac{e^{-i(\gamma\xi-n\pi)}}{\gamma\xi}. \qquad (18)$$

Also, we let $\eta = \cos\theta$, $\gamma = kd$ and $\xi = r/d$, and $d = a\sqrt{1-q^2}$ so that the far-field pressure at a distance r and off-axis angle θ from the hemispheroid is

$$\tilde{p}(r,\theta)|_{r\to\infty} = ika^2\rho_0 c\tilde{u}_0 \frac{e^{-ikr}}{2r}D(\theta), \qquad (19)$$

where

$$D(\theta) = -i\frac{2\sqrt{1-q^2}}{ka}\sum_{n=0}^{N}\frac{(-1)^n(4n+1)I_{2n}(-i\gamma)}{S'^{(4)}_{2n}(-i\gamma, i\xi_{ab})}$$
$$\times ps_{2n}(-i\gamma, \cos\theta). \qquad (20)$$

The far-field on-axis response is given by

$$D(0) = -i\frac{2\sqrt{1-q^2}}{ka}\sum_{n=0}^{N}\frac{(-1)^n(4n+1)I_{2n}(-i\gamma)}{S'^{(4)}_{2n}(-i\gamma, i\xi_{ab})}$$
$$\times ps_{2n}(-i\gamma, 1). \qquad (21)$$

As q approaches unity, the expansions in the spheroidal functions need fewer terms until we have a hemisphere, in which case the directivity is given by[3]

$$D(\theta)_{b=a}| = -i\frac{2}{ka}\sum_{n=0}^{N}\frac{(-1)^n(4n+1)P_{2n}(0)P_{2n}(\cos\theta)}{(2n-1)(2n+2)h'^{(2)}_{2n}(ka)}, \qquad (22)$$

where

$$h'^{(2)}_{2n}(ka) = ka\frac{2nh^{(2)}_{2n-1}(ka)-(2n+1)h^{(2)}_{2n+1}(ka)}{4n+1}. \qquad (23)$$

The on-axis pressure $20\log_{10}|D(0)|$ of the oblate hemispheroid for four values of q is plotted in Fig. 6, where we set the expansion limits to $N = 10 + 2\gamma$ and $R = 1.5\ N$. Compared to those of the spherical cap, shown in Fig. 3, these plots are clearly much smoother and the deep nulls, seen for the smaller angles, are virtually absent here. We define the angle β by

$$\beta = \arctan(b/a) = \arctan(q). \qquad (24)$$

The directivity pattern $20\log_{10}(|D(\theta)|/|D(0)|)$ is plotted for $\beta = 45°$ in Fig. 7(a), $\beta = 30°$ in Fig. 8(a), and $\beta = 15°$ in Fig. 9(a).

D. Radiation impedance

The total radiation force on one side is given by the integral of the normal component of the pressure over the surface,
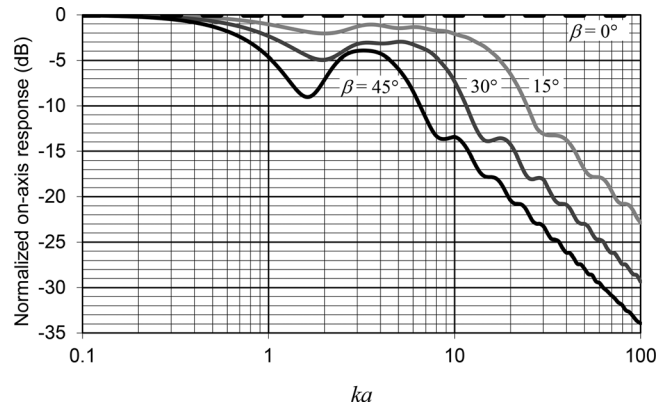

FIG. 6. On-axis pressure of an oblate hemispheroid in an infinite baffle for $\beta = 0°$, $15°$, $30°$, and $45°$ or $q = 0$, 0.268, 0.577, and 1, respectively.

$$\tilde{F} = \frac{1}{2}\int_0^{2\pi}\int_{-1}^{1}|\eta|\sqrt{\frac{\xi_{ab}^2+1}{\xi_{ab}^2+\eta^2}}\tilde{p}(\xi_{ab},\eta)dS, \qquad (25)$$

where we use the area element

$$dS = d^2\sqrt{(\xi_{ab}^2+1)(\xi_{ab}^2+\eta^2)}d\eta d\phi. \qquad (26)$$

Then the impedance is given by

$$Z_S = \frac{\tilde{F}}{\tilde{U}_0} = \frac{\tilde{F}}{\pi a^2\tilde{u}_0} = \frac{1}{\tilde{u}_0}\int_{-1}^{1}\tilde{p}(\xi_{ab},\eta)|\eta|d\eta$$
$$= -2\gamma\rho_0 c\sum_{n=0}^{\infty}(4n+1)I_{2n}^2(-i\gamma)\frac{S_{2n}^{(4)}(-i\gamma, i\xi_{ab})}{S'^{(4)}_{2n}(-i\gamma, i\xi_{ab})}, \qquad (27)$$

where we have again applied the integral identity of Eq. (16). The normalized radiation resistance R_R is given by

$$\boldsymbol{R}_S = \Re(Z_S) \qquad (28)$$

and the radiation reactance X_R by

$$X_R = \Im(Z_S). \qquad (29)$$

The normalized radiation resistance and reactance are plotted in Fig. 10 for four values of β. As q approaches unity, the power series in the spheroidal functions need fewer terms until we have a hemisphere, in which case the impedance is given by[3]

$$Z_s|_{b=a} = -2ika\rho_0 c\sum_{n=0}^{\infty}\frac{(4n+1)(P_{2n}(0))^2 h^{(2)}_{2n}(ka)}{(2n-1)^2(2n+2)^2 h'^{(2)}_{2n}(ka)}. \qquad (30)$$

On the other hand, as q approached zero, more terms are needed as the impedance converges towards that of a planar circular piston in an infinite baffle[3]

$$Z_S|_{b=0} = \rho_0 c\left(1 - \frac{J_1(2ka)}{ka} + i\frac{\mathbf{H}_1(2ka)}{ka}\right). \qquad (31)$$

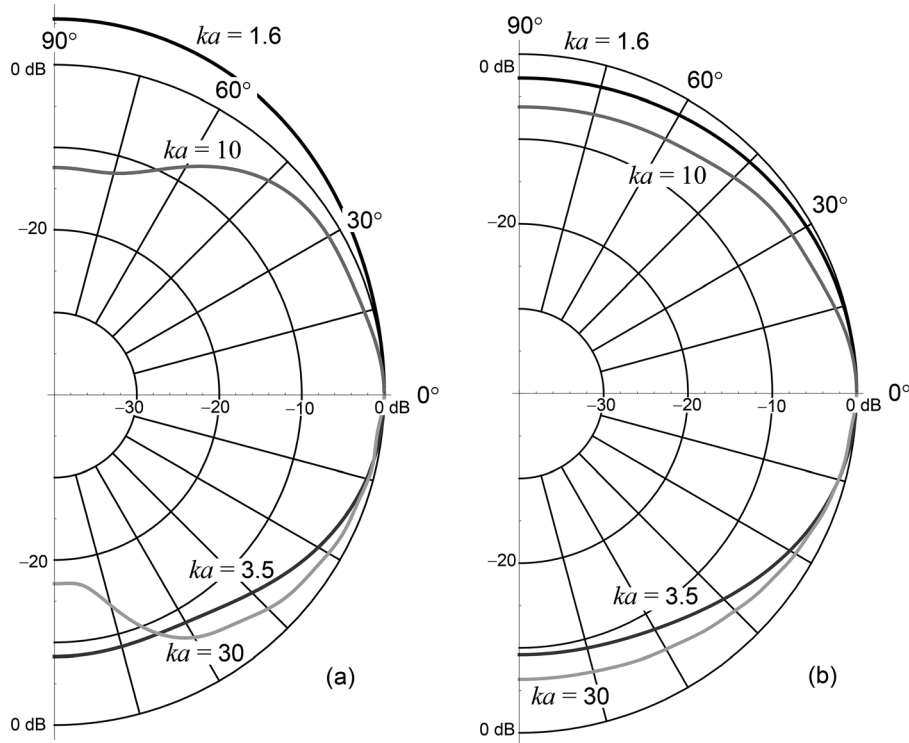J. Acoust. Soc. Am. **150** (4), October 2021

Tim Mellow and Leo Kärkkäinen   3051

FIG. 7. Directivity patterns 20 $\log_{10}(|D(\theta)|/|D(0)|)$ of the far-field pressure for an oblate hemispheroid where $\beta = 45°$ (a) and the high-frequency approximation (b).

E. Discussion

We see that for the smaller angles $\beta = 15°$ and $30°$, the radiation is contained largely within the half-cone angle β at higher frequencies ($ka \geq 10$), but for $\beta = 45°$ it extends to around $60°$. From Fig. 6, we see that there is a pronounced first dip in the on-axis response of the hemisphere ($\beta = 45°$) at $ka = 1.6$, which is less pronounced for the hemispheroids. This

leads to a broadening of the directivity pattern in Fig. 7(a) because there is less of a dip off axis. Conversely, we see a narrowing of the pattern corresponding to the on-axis peak at $ka = 3.5$. We see from the radiation resistance in Fig. 10 that the total radiated power shows no fluctuation in this region. These effects are less visible in the directivity patterns of Figs. 8(a) and 9(a) for the $30°$ and $15°$ hemispheroids, respectively.
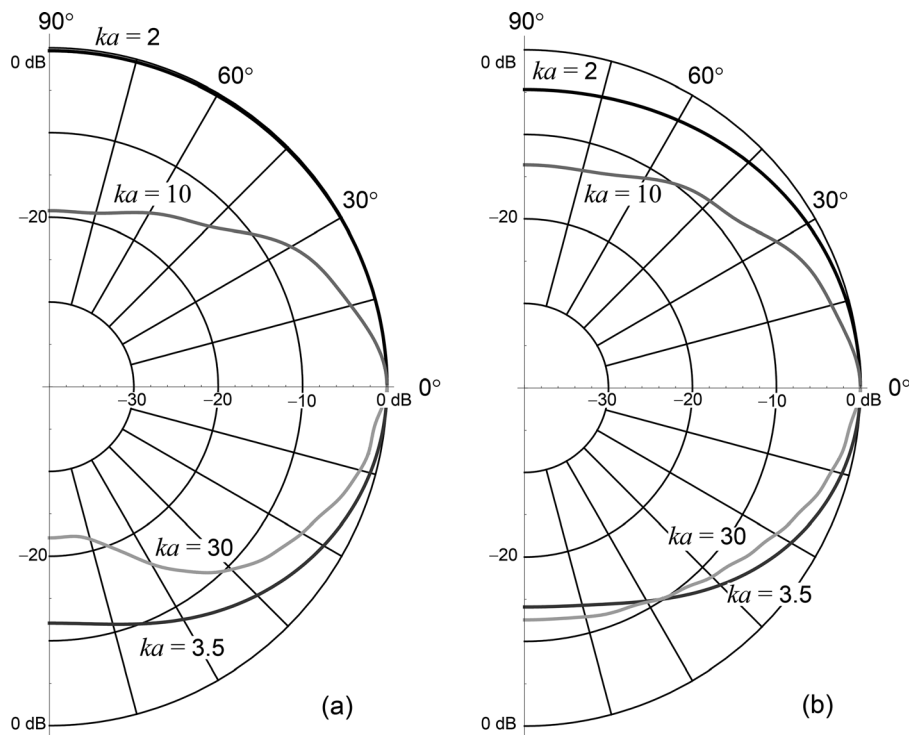

FIG. 8. Directivity patterns 20 $\log_{10}(|D(\theta)|/|D(0)|)$ of the far-field pressure for an oblate hemispheroid where $\beta = 30°$ (a) and the high-frequency approximation (b).
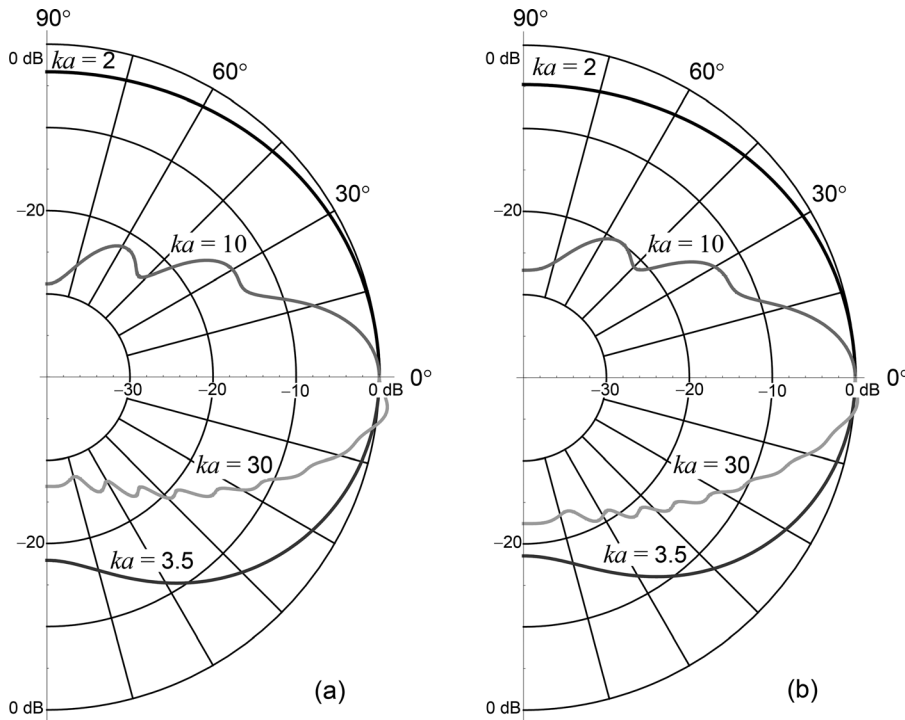
Tim Mellow and Leo Kärkkäinen

FIG. 9. Directivity patterns $20 \log_{10}(|D(\theta)|/|D(0)|)$ of the far-field pressure for an oblate hemispheroid where $\beta = 15°$ (a) and the high-frequency approximation (b).

F. High-frequency approximation

A similar approximation to that derived by Kates[1] for the spherical cap may be used for the oblate hemispheroid. This is achieved by mapping the hemispheroid onto the plane of the baffle and applying a time delay that compensates for the time lag between any point surface of the spheroid and its apex. Let an area mapping factor be the ratio between the area of an element on the spheroid dS, as given by Eq. (26), and the corresponding area projected onto the plane of the baffle $dS|_{\xi_{ab}=0}$,

$$\frac{dS}{dS|_{\xi_{ab}=0}} = \frac{\sqrt{(\xi_{ab}^2 + 1)(\xi_{ab}^2 + \eta^2)}}{\eta}. \quad (32)$$

Similarly, we must scale the velocity by the normal component from the third line of Eq. (9). Multiplying these two factors together gives

$$\frac{\tilde{u}(\xi_{ab}, \eta)dS}{\tilde{u}_0 dS|_{\xi_{ab}=0}} = \xi_{ab}^2 + 1 = \frac{a^2}{a^2 - b^2}, \quad (33)$$

which is just a constant, independent of η. The far-field pressure of a planar circular radiator in an infinite baffle with an arbitrary radial surface velocity distribution $\tilde{u}_+(w)$, where w and z are the radial and axial ordinates, respectively, is given by the monopole Rayleigh integral, taking into account the double strength source[3]

$$\tilde{p}(r, \theta)|_{r \to \infty} = i2k\rho_0 c \int_{-\pi}^{\pi} \int_0^a \tilde{u}_+(w_0)$$
$$\times g(r, \theta, \phi|w_0, \phi_0, z_0)|_{z_0=0+} w_0 dw_0 d\phi_0$$
$$= ika^2 \rho_0 c \tilde{u}_0 \frac{e^{-ikr}}{2r} D(\theta), \quad (34)$$

where the far-field Green's function in spherical–cylindrical coordinates is given by[3]

$$g(r, \theta, \phi|w_0, \phi_0, z_0)|_{r \to \infty} = \frac{e^{-ikr}}{4\pi r} e^{ik(w_0 \sin\theta \cos(\phi - \phi_0) + z_0 \cos\theta)}. \quad (35)$$

To approximate an oblate hemispheroid with a cross section described by Eq. (1), using a planar radiator, we set the surface velocity to have a radially varying time delay
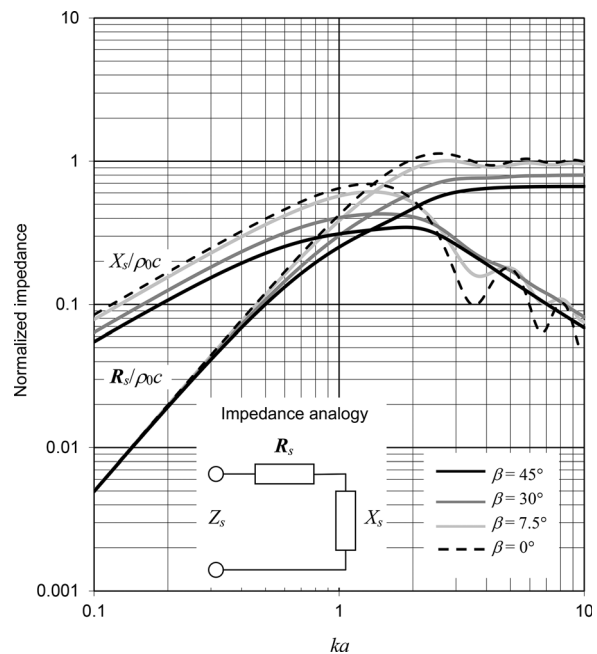

FIG. 10. Normalized radiation resistance and reactance of an oblate hemispheroid in an infinite baffle for $\beta = 0°$, 7.5°, 30°, and 45° or $q = 0$, 0.132, 0.577, and 1, respectively.

J. Acoust. Soc. Am. **150** (4), October 2021

Tim Mellow and Leo Kärkkäinen   3053

$$T(w_0) = \frac{b}{c}\left(1 - \sqrt{1 - \frac{w_0^2}{a^2}}\right), \quad 0 \le w_0 \le a, \qquad (36)$$

as shown in Fig. 11, so that the surface velocity becomes

$$\tilde{u}_+(w_0) = \tilde{u}_0 e^{-i\omega T(w_0)}. \qquad (37)$$

Inserting Eqs. (35) and (37) into Eq. (34) and integrating over ϕ_0 yields the directivity function

$$D(\theta) = \frac{2}{a^2} \int_0^a e^{-i\omega T(w_0)} J_0(kw_0 \sin\theta) w_0 dw_0, \qquad (38)$$

where we have used the integral identity[10]

$$\int_{-\pi}^{\pi} e^{iz\cos(\phi-\phi_0)} d\phi_0 = 2\pi J_0(z). \qquad (39)$$

If we insert Eq. (36) into Eq. (38) and let $w_0 = at$, this simplifies to

$$D(\theta) = 2 \int_0^1 e^{-ikb\left(1-\sqrt{1-t^2}\right)} J_0(kat\sin\theta) t dt. \qquad (40)$$

We may evaluate the integral over t in Eq. (40) for $\theta = 0$ using the integral identity

$$\int_0^1 e^{-ikb\left(1-\sqrt{1-t^2}\right)} t dt = \frac{1}{k^2 b^2}\left(1 - e^{-ikb} - ikb\right). \qquad (41)$$

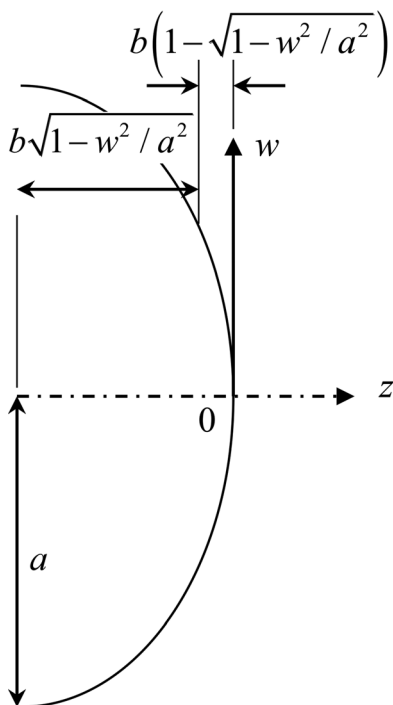Hence, the on-axis pressure is given by the simple closed-form formula

$$D(0) = \frac{2}{q^2 k^2 a^2}\left(1 - e^{-iqka} - iqka\right), \qquad (42)$$

which is plotted in Fig. 12 using $20\log_{10}|D(0)|$ for four values of q. We see that the frequency response shape is independent of the height b. The roll-off simply moves up in frequency as the height is reduced. The -4 dB point is given by

$$ka|_{-4dB} = \frac{4}{q}. \qquad (43)$$

This also holds for $q > 1$, where we have the high-frequency approximation of a prolate spheroid. Compared to the on-axis responses of the physical hemispheroid shown in Fig. 6, we see that the first dip of each plot, immediately above the roll-off, is smoothed out by the high-frequency approximation. This is also true of Kates' approximation of a spherical cap.[1] The directivity pattern $20\log_{10}(|D(\theta)|/|D(0)|)$ is plotted for $\beta = 45°$ in Fig. 7(b), $\beta = 30°$ in Fig. 8(b), and $\beta = 15°$ in Fig. 9(b).

Comparing these to the directivity patterns of the physical hemispheroid plotted in Figs. 7(a), 8(a) and 9(a), we see that in the case of $\beta = 15°$, the correlation between the two is remarkably good except that the physical hemispheroid shows slightly greater rejection of sound radiated near 90° off axis at higher frequencies.

III. FAR-FIELD PRESSURE OF A PROLATE HEMISPHEROID USING A HIGH-FREQUENCY APPROXIMATION

A. Far-field pressure

The oblate hemispheroid only allows the directivity to be determined over all azimuthal angles ϕ simultaneously. A useful alternative is the hemi-ellipsoid shown in Fig. 13, which has a height h and an elliptic outline, of major and minor radii a and b, respectively, defined in rectangular coordinates (x, y) by
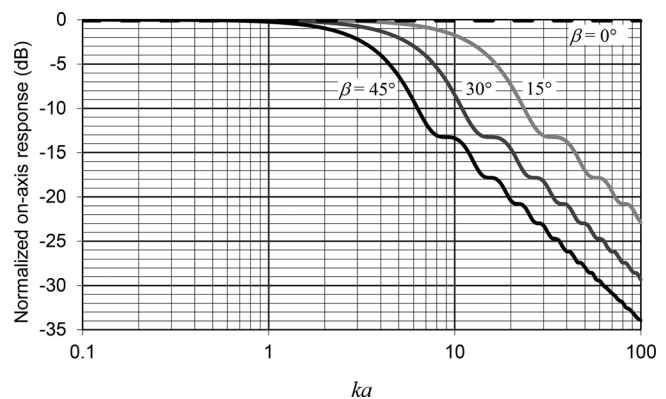
FIG. 11. Delay path length for the oblate hemispheroid.

FIG. 12. On-axis pressure of an oblate hemispheroid in an infinite baffle for $\beta = 0°$, 15°, 30°, and 45° or $q = 0$, 0.268, 0.577, and 1, respectively, using the high-frequency approximation of Eq. (42).
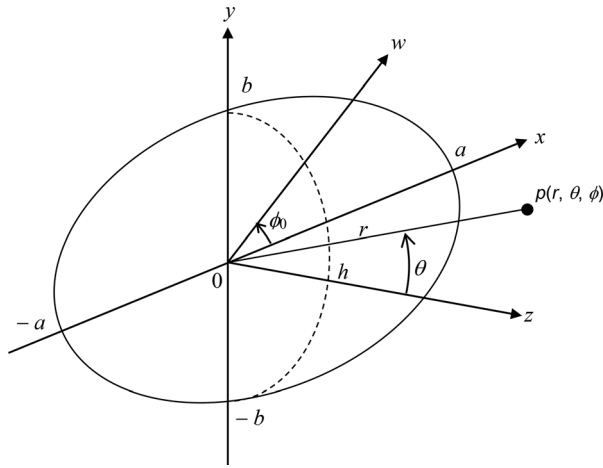
Tim Mellow and Leo Kärkkäinen

FIG. 13. Geometry of a hemi-ellipsoid in infinite baffle.

$$y = \pm b \sqrt{1 - \frac{x^2}{a^2}}, \quad -a \leq x \leq a. \tag{44}$$

The cross section is semi-elliptic and it offers the possibility of different directivity patterns in the xz- and yz-planes. To derive the far-field pressure of the physical hemi-ellipsoid would be overly complicated using ellipsoidal functions, but we may derive a high-frequency approximation assuming a planar radiator with a radially varying delay, as we did for the oblate hemispheroid. For the plots, however, we will simplify things further by letting $h = b$ so that we have a prolate hemispheroid with a semicircular cross section in the yz-plane. The far-field pressure of the planar elliptic radiator in an infinite baffle with an arbitrary radial surface velocity distribution $\tilde{u}_+(x_0, y_0)$ is given by the monopole Rayleigh integral,[3] taking into account the double strength source

$$\tilde{p}(r, \theta, \phi)|_{r \to \infty} = i2k\rho_0 c \int_{-a}^{a} \int_{-b\sqrt{1-x_0^2/a^2}}^{b\sqrt{1-x_0^2/a^2}} \tilde{u}_+(x_0, y_0)$$
$$\times g(r, \theta, \phi | x_0, y_0, z_0)|_{z_0=0+} dy_0 dz_0$$
$$= ikab\rho_0 c \tilde{u}_0 \frac{e^{-ikr}}{2r} D(\theta, \phi), \tag{45}$$

where the far-field Green's function in spherical–rectangular coordinates is obtained by substituting $x = r \sin\theta \cos\phi$, $y = r \sin\theta \sin\phi$, and $z = r \cos\theta$ in the far-field Green's function in rectangular coordinates[3]

$$g(r, \theta, \phi | x_0, y_0, z_0)|_{z_0=0} = \frac{e^{-ikr}}{4\pi r} e^{ik\sin\theta(x_0\cos\phi + y_0\sin\phi)} \tag{46}$$

to give

$$D(\theta, \phi) = \frac{1}{\pi ab \sim u_0} \int_{-a}^{a} \int_{-b\sqrt{1-x_0^2/a^2}}^{b\sqrt{1-x_0^2/a^2}}$$
$$\sim u_+(x_0, y_0) e^{ik\sin\theta(x_0\cos\phi + y_0\sin\phi)} dx_0 dy_0. \tag{47}$$

In cylindrical coordinates (ρ, ϕ_0), we let $x_0 = a\rho \cos\phi_0$ and $y_0 = b\rho \sin\phi_0$. This maps the integral onto a unit circle[11] as follows:

$$D(\theta, \phi) = \frac{1}{\pi \tilde{u}_0} \int_{-\pi}^{\pi} \int_0^1 \tilde{u}_+(\rho) e^{ik\rho \sin\theta(a\cos\phi\cos\phi_0 + b\sin\phi\sin\phi_0)}$$
$$\times \rho d\rho d\phi_0. \tag{48}$$

To emulate a hemi-ellipsoid, with an outline described by Eq. (1), we set the surface velocity to have a radially varying time delay

$$T(\rho) = \frac{h}{c}\left(1 - \sqrt{1 - \rho^2}\right), \quad 0 \leq \rho \leq 1 \tag{49}$$

in a similar manner to that already shown in Fig. 11, so that the surface velocity becomes

$$\tilde{u}_+(\rho) = \tilde{u}_0 e^{-i\omega T(\rho)}. \tag{50}$$

Applying the identity[10] $\arctan x = \arccos\left(1/\sqrt{1 + x^2}\right) = \arcsin\left(x/\sqrt{1 + x^2}\right)$ so that

$$\cos\Phi = \frac{a\cos\phi}{\sqrt{a^2\cos^2\phi + b^2\sin^2\phi}}, \tag{51}$$

$$\sin\Phi = \frac{b\sin\phi}{\sqrt{a^2\cos^2\phi + b^2\sin^2\phi}}, \tag{52}$$

$$\cos\Phi\cos\phi_0 + \sin\Phi\sin\phi_0 = \cos(\Phi - \phi_0), \tag{53}$$

where

$$\Phi = \arctan\left(\frac{b}{a}\tan\phi\right) \tag{54}$$

leads to

$$D(\theta, \phi) = \frac{1}{\pi} \int_{-\pi}^{\pi} \int_0^1 e^{-ikh\left(1 - \sqrt{1-\rho^2}\right)}$$
$$\times e^{ik\rho\sin\theta\sqrt{a^2\cos^2\phi + b^2\sin^2\phi}\cos(\Phi-\phi_0)} \rho d\rho d\phi_0. \tag{55}$$

Applying the integral identity of Eq. (39) again yields

$$D(\theta, \phi) = 2\int_0^1 e^{-ikh\left(1 - \sqrt{1-\rho^2}\right)}$$
$$\times J_0\left(k\rho\sin\theta\sqrt{a^2\cos^2\phi + b^2\sin^2\phi}\right)\rho d\rho. \tag{56}$$

If we calculate the directivity using numerical integration, we find that we have the directivity pattern of an axisymmetric oblate hemispheroid of height h and radius a when $\phi = 0$ and radius b when $\phi = \pi/2$. Not surprisingly, this confirms that the directivity in each plane may be controlled independently. This may be illustrated by setting $h = 0$ in Eq. (56) so that we have a planar elliptic piston in an infinite baffle. Applying the integral identity

J. Acoust. Soc. Am. **150** (4), October 2021

Tim Mellow and Leo Kärkkäinen   3055

$$\int_0^1 J_0(\rho z) \rho \, d\rho = \frac{J_1(z)}{z} \qquad (57)$$

yields the renowned directivity pattern of an elliptic piston[11,12] given by

$$D(\theta, \phi)|_{h=0} = \frac{2J_1\left(k \sin\theta \sqrt{a^2 \cos^2\phi + b^2 \sin^2\phi}\right)}{k \sin\theta \sqrt{a^2 \cos^2\phi + b^2 \sin^2\phi}}. \qquad (58)$$

We see that this gives the same directivity pattern as that of a circular piston[3] of radius a when $\phi = 0$ and radius b when $\phi = \pi/2$. On axis, Eq. (56) reduces to

$$D(0, \phi) = 2\int_0^1 e^{-ikh\left(1-\sqrt{1-\rho^2}\right)} \rho \, d\rho$$
$$= \frac{2}{k^2 h^2}\left(1 - e^{-ikh} - ikh\right). \qquad (59)$$

If $h = b$ and $b = qa$, so that we have a prolate hemispheroid, this is identical to the on-axis directivity function of Eq. (42) for an oblate hemispheroid.

B. Steered array

For a steered directivity pattern in the horizontal x-z plane, we include an extra delay dependent on the steering angle ψ,

$$T(\rho, \phi_0) = \frac{b}{c}\left(1 - \sqrt{1-\rho^2}\right) - \frac{a}{c}\rho \cos\phi_0 \sin\psi,$$
$$\begin{cases} 0 \le \rho \le 1 \\ 0 \le \phi_0 \le 2\pi, \end{cases} \qquad (60)$$

which leads to the directivity function

$$D(\theta, \phi) = 2\int_0^1 e^{-ikh\left(1-\sqrt{1-\rho^2}\right)}$$
$$\times J_0\left(k\rho\left(\sin\theta\sqrt{a^2\cos^2\phi + b^2\sin^2\phi}\right.\right.$$
$$\left.\left. -a\sin\psi\right)\right)\rho \, d\rho. \qquad (61)$$

This is plotted in Fig. 14 for various steering angles ψ. We see that, although the steering works without introducing lobes, the pattern becomes somewhat asymmetrical for larger angles.

IV. CONCLUSION

We have shown that oblate spheroids can be used to give virtually any desired beam width without the lobes or on-axis nulls associated with a spherical cap, especially for narrower beam widths, where we can say, as a useful rule of thumb, that the directivity pattern is contained largely within the half-cone angle α for a spherical cap and β for an oblate hemispheroid. Obviously, the two converge in the limit where they both
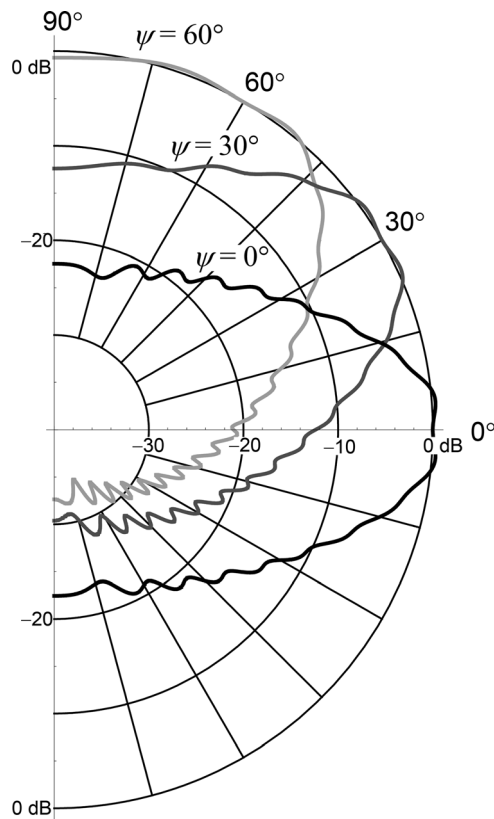

FIG. 14. Directivity patterns $20 \log_{10}(|D(\theta, 0)|/|D(\psi, 0)|)$ of the far-field pressure for a steered prolate hemispheroid with $ka = 30$ and $\beta = 15°$ or $q = 0.268$.

become hemispheres ($\alpha = 90°$ and $\beta = 45°$) with a half-cone angle of around $60°$ and so this rule breaks down.

The directivity patterns of the high-frequency approximation, using a planar source with a radially increasing delay, agree well with those of the physical spheroid except that the amount of sound radiated $90°$ of axis from the planar source is greater. The on-axis response of the planar source is given by a simple closed-form solution which smooths out the first dip due to the geometry of the physical spheroid.

We have also derived the far-field pressure of a hemi-ellipsoid, again using the high-frequency approximation, which potentially allows the directivity patterns in two perpendicular planes to be determined independently. We have shown that in the case where the dome height is the same as the smallest outline radius (so that we have a prolate hemispheroid), the directivity patterns agree well with those of the corresponding oblate hemispheroids of the same internal angles β in each plane.

Finally, we have shown that applying a radially increasing delay with an elliptic cross section is not only a viable method for controlling the beam width, but the beam may also be steered by applying a further delay that increases linearly from one edge to the opposite one.

The elliptic cross section appears to be a rather effective alternative to a shaded array as a means of apodization and is more efficient because, unlike a shaded array, constant

Tim Mellow and Leo Kärkkäinen

axial velocity is maintained over the whole surface. It is "self-shading" due to its geometry.

ACKNOWLEDGMENTS

APPENDIX: AXISYMMETRIC OBLATE SPHEROIDAL WAVE FUNCTIONS

The radial and angular oblate spheroidal wave functions $S_n^{(p)}$ and ps_n are solutions to the following radial and angular wave equations, respectively,

$$\left\{\frac{\partial}{\partial \xi}\left((\xi^2+1)\frac{\partial}{\partial \xi}\right)+\gamma^2(\xi^2+1)-\lambda_n(\gamma)\right\}S_n^{(p)}(-i\gamma,i\xi)=0,$$
(A1)

$$\left\{\frac{\partial}{\partial \eta}\left((1-\eta^2)\frac{\partial}{\partial \eta}\right)-\gamma^2(1-\eta^2)+\lambda_n(\gamma)\right\}\mathrm{ps}_n(-j\gamma,\eta)=0,$$
(A2)

in which, due to axial symmetry, we have set the azimuthal constant of separation m (or μ) $=0$. The functions are defined by

$$S_n^{(p)}(-i\gamma,i\xi)=\rho_n(-i\gamma)\sum_{r=-\lfloor n/2\rfloor}^{N}u_{n,r}(-i\gamma)$$
$$\times \begin{cases} j_{n+2r}(\gamma\xi), & p=1 \\ y_{n+2r}(\gamma\xi), & p=2 \\ h_{n+2r}^{(1)}(\gamma\xi), & p=3 \\ h_{n+2r}^{(2)}(\gamma\xi), & p=4, \end{cases}$$
(A3)

$$\mathrm{ps}_n(-i\gamma,\eta)=\sigma_n(-i\gamma)\sum_{r=-\lfloor n/2\rfloor}^{N}(-1)^r u_{n,r}(-i\gamma)P_{n+2r}(\eta),$$
(A4)

where λ_n are the eigenvalues, ρ_n and σ_n are the radial and angular normalizing factors, respectively, $h_{n+2r}^{(2)}$ are spherical Hankel functions of the second kind, P_{n+2r} are Legendre functions of the first kind, and $u_{n,r}$ are the expansion coefficients defined by the recursion formulas

$$u_{n,r}(\gamma)=1, \quad r=-\lfloor n/2\rfloor,$$
(A5)

$$u_{n,r}(\gamma)=N_{n,r}(\gamma)u_{n,r-1}(\gamma), \quad r>-\lfloor n/2\rfloor,$$
(A6)

where

$$N_{n,r}(\gamma)=V_{n,p}(\gamma)|_{p=r}$$
(A7)

is a continued fraction obtained by tabulating $V_{n,p}$ from $p=R$ to r in steps of -1 using the formulas

$$V_{n,p}(\gamma)=-\frac{C_{n,N}(\gamma)}{B_{n,N}(\gamma)+\lambda_n(\gamma)}, \quad p=R,$$
(A8)

$$V_{n,p}(\gamma)=-\frac{C_{n,p}(\gamma)}{B_{n,p}(\gamma)+\lambda_n(\gamma)+A_{n,p}(\gamma)V_{n,p+1}(\gamma)}, \quad p<R,$$
(A9)

where

$$A_{n,r}(\gamma)=-\gamma^2\frac{(n+2r+1)(n+2r+2)}{(2n+4r+3)(2n+4r+5)},$$
(A10)

$$B_{n,r}(\gamma)=-\frac{\gamma^2}{2}\left(1-\frac{1}{(2n+4r-1)(2n+4r+3)}\right)$$
$$-(n+2r)(n+2r+1),$$
(A11)

$$C_{n,r}(\gamma)=-\gamma^2\frac{(n+2r-1)(n+2r)}{(2n+4r-3)(2n+4r-1)}.$$
(A12)

The eigenvalues $\lambda_n(\gamma)$ are found from the matrix equation[13]

$$|\mathbf{M}-\lambda\mathbf{I}|=0,$$
(A13)

where $\mathbf{I}$ is the identity matrix and the elements of the tridiagonal matrix $\mathbf{M}$ are given by

$$\mathbf{M}_{p,q}(n,\gamma)=\delta_{p,q+1}C_{n,p}(\gamma)-\delta_{p,q}B_{n,p}(\gamma)+\delta_{p+1,q}A_{n,p}(\gamma),$$
$$\begin{cases} 0\le p\le\lfloor 3R/2\rfloor \\ 0\le q\le\lfloor 3R/2\rfloor, \end{cases}$$
(A14)

where $\delta_{p,q}$ is the Kronecker delta function. Hence, the problem is reduced to one of finding the eigenvalues of the matrix $\mathbf{M}$. Then the vector $\mathbf{e}(n,\gamma)$ is the list of eigenvalues of the matrix $\mathbf{M}$ in ascending order and, as above, we have

$$\lambda_n(\gamma)=\mathbf{e}_{\lfloor n/2\rfloor}(\varepsilon(n),\gamma), \quad \varepsilon(n)=\begin{cases} 1, & n\,\mathrm{odd} \\ 0, & n\,\mathrm{even}. \end{cases}$$
(A15)

We have chosen unity for the starting values of the coefficients in Eq. (A5) quite arbitrarily because the absolute values of the spheroidal functions will be determined by the normalization factors chosen. The radial normalization factor is chosen so that for large arguments, the radial spheroidal function converges to a spherical Hankel function

$$S_n^{(4)}(-j\gamma,j\xi)|_{\xi\to\infty}=h_n^{(2)}(\gamma\xi)|_{\xi\to\infty}=j\frac{e^{-j(\gamma\xi-n\pi/2)}}{\gamma\xi}.$$
(A16)

Hence

$$\rho_n(\gamma)=\left(\sum_{r=-\lfloor n/2\rfloor}^{R}(-1)^r u_{n,r}(\gamma)\right)^{-1}.$$
(A17)

For the angular functions, there are three possible normalization schemes. In the scheme by Flammer,[5] the angular spheroidal function converges to a Legendre function when the argument is zero

$$S_n^{(1)}(-ic,0) = P_n(0), \tag{A18}$$

whereas in the one by Stratton *et al.*,[6] this happens when the argument is unity,

$$S_n^{(1)}(-ic,0) = P_n(1). \tag{A19}$$

However, the scheme we use is the one by Meixner *et al.*[7] in which the orthogonal integral of a pair of angular spheroidal functions between -1 and 1 gives the same result as a pair of Legendre functions[10]

$$\int_{-1}^{1} \mathrm{ps}_m(-j\gamma,\eta)\mathrm{ps}_n(-j\gamma,\eta)d\eta = \int_{-1}^{1} P_m(\eta)P_n(\eta)d\eta$$
$$= \begin{cases} 0, & m \neq n \\ \dfrac{2}{2n+1}, & m = n. \end{cases} \tag{A20}$$

Hence

$$\sigma_n(\gamma) = \left((2n+1) \sum_{r=-\lfloor n/2 \rfloor}^{R} \frac{\left(u_{n,r}(\gamma)\right)^2}{2n+4r+1} \right)^{-1/2}. \tag{A21}$$

[1]J. M. Kates, "Radiation from a dome," J. Audio Eng. Soc. **24**(9), 735–737 (1976).

[2]H. Suzuki and J. Tichy, "Sound radiation from convex and concave domes in an infinite baffle," J. Acoust. Soc. Am. **69**(1), 41–49 (1981).

[3]L. L. Beranek and T. J. Mellow, *Acoustics: Sound Fields, Transducers, and Vibration*, 2nd ed. (Academic Press, London, 2019), pp. 577–814.

[4]P. J. Walker, "New developments in electrostatic loudspeakers," J. Audio Eng. Soc. **28**(11), 795–799 (1980).

[5]C. Flammer, *Spheroidal Wave Functions* (Stanford University Press, Stanford, CA, 1957), pp. 21–22.

[6]J. A. Stratton, P. M. Morse, L. J. Chu, J. D. C. Little, and F. J. Corbató, *Spheroidal Wave Functions* (John Wiley & Sons, Inc., New York, 1956), pp. 56–58.

[7]J. Meixner and F. W. Schäfke, *Mathieusche Funktionen Und Sphäroidfunktionen* (*Mathieu Functions and Spheroidal Functions*) (Springer-Verlag, Berlin, Göttingen, Heidelberg, Germany, 1954), pp. 283–300 (in German).

[8]P. E. Falloon, P. C. Abbott, and J. B. Wang, "Theory and computation of spheroidal wavefunctions," J. Phys. A-Math. Gen. **36**(20), 5477–5495 (2003).

[9]A. L. Van Buren, "Accurate calculation of oblate spheroidal wave functions," arXiv:1708.07929 (2019).

[10]I. S. Gradshteyn and I. M. Ryzhik, *Table of Integrals, Series, and Products*, 6th ed., edited by A. Jeffrey (Academic, New York, 2000), p. 55, Eqs. (1.624.7) and (1.624.8); p. 668, Eq. (6.561.5); p.762, Eq. (7.112.1); p. 764, Eq. (7.126.1); p. 888, Eqs. (8.339.2) and (8.339.3); and p. 902, Eq. (8.411.7).

[11]H. Stenzel, "Über die akustische Strahlung von Membranen (On the acoustic radiation from membranes)," Ann. Phys. **399**(8), 947–982 (1930) (in German).

[12]F. P. Mechel (Ed.), *Formulas of Acoustics*, 1st ed. (Springer, New York, 2002), p. 229.

[13]D. B. Hodge, "Eigenvalues and eigenfunctions of the spheroidal wave function," J. Math. Phys. **11**(8), 2308–2312 (1970).

Tim Mellow and Leo Kärkkäinen